

Formation Process of Na_3SbS_4 Solid Electrolyte via a Liquid-Phase Reaction Using Acetonitrile

Yayu Guo,^[a] Xixi Shi,*^[a] Yue Ma,^[a] Dawei Song,*^[a] Hongzhou Zhang,^[a] Chunliang Li,^[a] and Lianqi Zhang^[a]

Antimony-based sulfide solid electrolyte Na_3SbS_4 with good moisture stability is attractive for practical application in all-solid-state sodium batteries. Liquid-phase reaction is a facile and widely-used strategy, but the specific reactions in synthetic process and related mechanisms are still unclear. Herein, the reaction processes of synthesizing Na_3SbS_4 by liquid-phase reaction of Na_2S , Sb_2S_3 and S in acetonitrile (ACN) are extensively investigated. A colorless supernatant and dark green precipitate are obtained after reacting for 24 h, the raw

materials are negligible in supernatant. More importantly, the post-treatment temperature is investigated and the tetragonal Na_3SbS_4 ($t\text{-Na}_3\text{SbS}_4$) with high ionic conductivity (0.46 mS cm^{-1} at 25°C) is obtained after heating at 450°C for 3 h. Remarkably, the direct stacking of electrolyte is developed and $t\text{-Na}_3\text{SbS}_4$ is further prepared into a free-standing sheet-type solid electrolyte membrane using polytetrafluoroethylene (PTFE) fibrillation, then an ionic conductivity is achieved (0.17 mS cm^{-1} at 25°C).

Introduction

Various advanced energy storage technologies have been developed due to the growing demand for sustainable energy storage. Especially, lithium-ion batteries (LIBs) afford great breakthroughs, however, the limited resource and the geologically uneven distribution of Li impede the sustainable development of LIBs. Sodium-ion batteries (SIBs) with rich reserves of sodium are promising candidates to address these issues. Specially, the all-solid-state sodium-ion batteries using non-flammable inorganic solid sulfide electrolytes are emerging as promising solutions to address the safety issues associated with flammable organic liquid electrolytes since sulfide solid electrolytes (SSEs) present the advantages of rare leakage, high ionic conductivity, low sintering temperature and negligible grain boundary resistance, fulfilling most criteria for high-performance solid electrolytes.^[1–10]

Liquid-phase reaction using solvent as media presents advantages in preparing SSEs including low cost, easily manageable and good homogeneity.^[11–16] Moreover, in contrast to the conventional synthetic methods such as ball milling^[17,18] and high temperature solid phase reaction,^[19,20] the liquid-phase reaction is suitable for large-scale production. The liquid-phase reaction of preparing sodium-ion SSEs can be divided into two categories: (1) Liquid-phase reaction using organic

solvent: Precursor powders are slightly soluble in polar aprotic organic solvents such as acetonitrile (ACN), ethyl propionate, 1,2-dimethoxyethane, tetrahydrofuran, etc., to generate precipitate and response in the solvent,^[21–24] small and uniform particles are suggested be generated,^[23,25] which are conducive to the improvement of ionic conductivity in this liquid-phase reaction. (2) Aqueous solution method: the raw materials can be completely dissolved in deionized water and the sodium-ion SSEs such as Na_3SbS_4 ,^[12,26–28] $\text{Na}_{3+x}(\text{Sb}_{1-x}\text{Sn}_x)\text{S}_4$ ^[29] and $\text{Na}_3\text{SbS}_4\text{-Na}_2\text{WS}_4$ ^[30] can be synthesized. However, the separation from water to obtain electrolyte powder is difficult, and the impurities are facile to generate, which influences the property of electrolytes. It is worth noting that after above methods, the pretreated SSEs need further drying and subsequent heat treatments. Heat treatment is a necessary process to remove impurities such as unreacted raw materials and solvents after liquid-phase synthesis.^[14,21,38,39]

The Na_3SbS_4 sulfide electrolyte has attracted widespread concern due to the distinguished ionic conductivity ($1\text{--}3 \text{ mS cm}^{-1}$) at room temperature and high chemical stability under ambient conditions.^[31–36] Gamo et al.^[29,37] synthesize Na_3SbS_4 by aqueous solution method and after the reaction, the water is removed by adding acetone and $\text{Na}_3\text{SbS}_4\cdot 9\text{H}_2\text{O}$ is achieved after aging for 2 days, then high-temperature heating is conducted to prepare Na_3SbS_4 electrolyte. Cao et al.^[1] use ethanol to purify $\text{Na}_3\text{SbS}_4\cdot 9\text{H}_2\text{O}$ after aqueous solution reaction. Hence, preparing Na_3SbS_4 using aqueous solution approach is a cumbersome procedure, and not suitable for large-scale production. Liquid-phase reaction using organic solvent is efficient and operationally simple compared with other synthesis methods, which is favorable for large-scale production. However, the synthesis procedures are not consummate enough, and the chemical reaction mechanisms are not fully understood.

[a] Y. Guo, Prof. X. Shi, Dr. Y. Ma, Prof. D. Song, Prof. H. Zhang, Prof. C. Li, Prof. L. Zhang
School of Materials Science and Engineering, Tianjin University of Technology
Tianjin 300384, China
E-mail: cshi6@163.com
songdw2005@mail.nankai.edu.cn

 This publication is part of a joint Special Collection on Solid State Batteries, featuring contributions published in Advanced Energy Materials, Energy Technology, Batteries & Supercaps, ChemSusChem, and Advanced Energy and Sustainability Research.

In this work, ACN is chosen as the solvent for liquid-phase reaction to prepare the Na_3SbS_4 sulfide electrolyte precursor. The phase transition in this liquid-phase reaction is tracked, and the reaction mechanism of the heat treatment is subsequently investigated. The XRD results show that the products in the liquid-phase reaction using ACN are all in the precipitation, and the supernatant is only pure ACN. In contrast, the precipitations are not only Na_3SbS_4 but also include unreacted raw materials. Therefore, synthetic reactions also occur in further heat treatment. Eventually, Na_3SbS_4 electrolyte with evenly distributed small particles and high ionic conductivity is formed. To clarify the air stability of Na_3SbS_4 , the property exposed to air is also investigated using XRD patterns. More importantly, converting powdered solid electrolytes into sheet types, and compressing different cell components together are expected to facilitate the commercial production of batteries. Therefore, a free-standing electrolyte membrane with good ductility including Na_3SbS_4 and polytetrafluoroethylene (PTFE) binder is innovatively fabricated by simply rolling, the ionic conductivity of 0.17 mS cm^{-1} is obtained.

Results and Discussion

Na_3SbS_4 is synthesized by liquid-phase reaction of Na_2S , Sb_2S_3 and S in acetonitrile (ACN), and subsequently followed by heat

treatment in a muffle furnace. Due to the moisture and oxygen sensitivity of sulfide compounds, all material preparation processes are performed in a glove box. After the dissolution of raw materials in ACN, the color of the solution changes from colorless to dark green, and subsequently to light bluish-green during magnetic stirring. Finally, the reaction products including colorless supernatant and dark green precipitate can be observed after quiescence (Figure 1a). The color variation of the supernatants at different reaction times is shown in Figure 1(b), in response to these variations, the gradual darkness of the color of precipitations can be observed (Figure 1c), which may correspond to the fully carried out of the reaction.

To investigate the liquid-phase reaction using ACN, the intermediate products during different stirring times are centrifuged and dried. The collected powder precipitates are tested using Raman and XRD characterizations. As shown in Figure 2(a), with the increasing of stirring and reaction time, the Raman peaks for Na_2S and S gradually decrease, while the Raman peaks for sodium polysulfides (the peaks at 132, 450 and 480 cm^{-1}) gradually increase. Meanwhile, the resonance peaks attributed to the Sb–S vibrations of the isolated SbS_4 group increase significantly (the peaks at 402, 382, and 359 cm^{-1} are assigned to the stretching vibration modes of Sb–S) after 24 h of reaction, confirming the successful partial formation of SbS_4 group. The diffraction peaks corresponding to sodium polysulfides and Na_3SbS_4 can also be observed in the

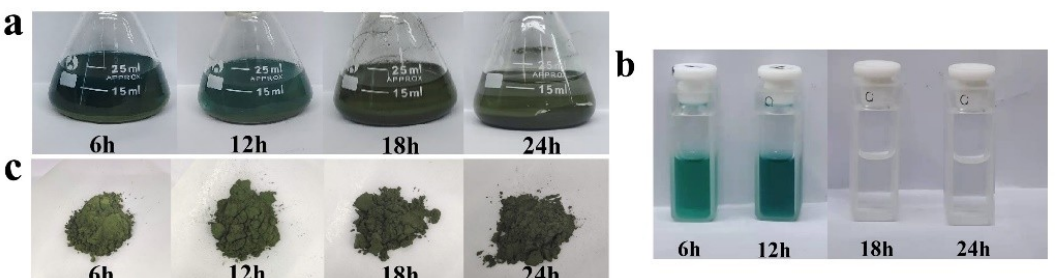


Figure 1. Optical photographs of liquid-phase reaction using ACN as solvent with different reaction times of 6, 12, 18 and 24 h, respectively. a) Mixture solutions, b) supernatants, and c) precipitates.

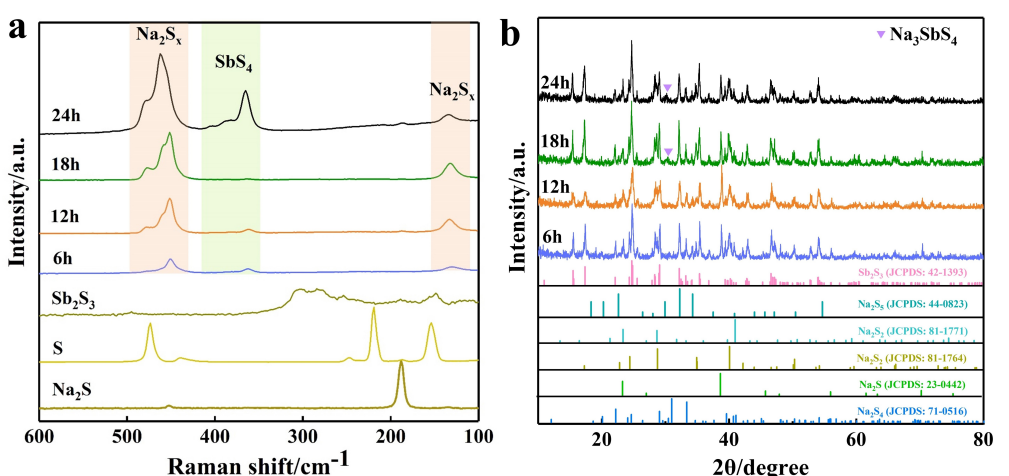


Figure 2. a) Raman spectra and b) XRD patterns of powder precipitates with different reaction times of 6, 12, 18 and 24 h after evaporation of ACN.

XRD results of Figure 2(b). The XRD results also indicate that unreacted raw material Sb_2S_3 is in the precipitation after liquid-phase reaction. Thus, only a small amount of raw materials in the precipitation transform to Na_3SbS_4 . Therefore, the final products of precipitation are mainly Sb_2S_3 , sodium polysulfide and a small amount of Na_3SbS_4 . Hence, it is anticipated that the synthesis reactions of Na_3SbS_4 will exist in the subsequent heat treatment.

To shed light on the thermal property of precursor in the heat-treatment process, DSC analysis is carried out from room temperature to 600°C and presented in Figure 3(a). Clear exothermic peaks at 302, 344, 435, and 549°C are observed in the DSC curve. Therefore, the precursor samples are heated from 300 to 600°C at every 50°C to explore the reaction of precursor during the heat treatment. The related XRD patterns are displayed in Figure 3(b), it should be noted that the peaks at $2\theta = 14.5^\circ$, 21.5° and 23.9° correspond to the peaks of Parafilm. When the heat treatment temperature reaches approximately 300 and 350°C, the raw materials Sb_2S_3 , NaS_2 , and intermediate products NaSbS_2 , NaS can be observed in addition to the electrolyte Na_3SbS_4 . When the temperature rises to 400°C, the aforementioned products become grey and completely transform into the tetragonal Na_3SbS_4 ($t\text{-Na}_3\text{SbS}_4$)^[31] indicating that the synthesis reactions of the precursor are complete at this temperature. When the temperature increases to 450°C, the characteristic peaks turn sharpened, indicating an increased level of $t\text{-Na}_3\text{SbS}_4$ crystallinity. Furthermore, some additional diffraction peaks appear when the annealing tem-

perature exceeds 500°C. The impurity phase ($2\theta = 27.2^\circ$ and 31.5°) appeared at the heat treatment temperatures of 500, 550 and 600°C is $\text{Na}_6\text{Sb}_4\text{S}_9$, which is due to the sublimation of sulfur and the presence of sulfur vacancies. The impurity phase ($2\theta = 32.3^\circ$, 34.1° and 45.0°) is identified as the Al_2O_3 of the crucible when the temperature reaches 600°C. The impedances of the corresponding products are also tested and the Nyquist plots are shown in Figure 3(c and d). The Nyquist plots indicate that the ionic conductivities increase with temperatures and a max value is obtained at 450°C, corresponding to the generation of high purity $t\text{-Na}_3\text{SbS}_4$. When the temperature is higher than 500°C, the ionic conductivity presents a decreasing trend, which implies the formation of impurities and consists with the result of XRD patterns.

The formation of $t\text{-Na}_3\text{SbS}_4$ is further verified by Rietveld refinement, and the result is shown in Figure 4(a). The halo patterns at the low angle match the polyimide film. The crystal structure of the as-synthesized $t\text{-Na}_3\text{SbS}_4$ sample (a , $b = 7.182919 \text{ \AA}$ and $c = 7.313156 \text{ \AA}$, $P2_1c$, no.114) is consistent with the theoretical calculation results. All XRD peaks are in good agreement with previously published values.^[31] Figure 4(b) shows the Raman spectrum of $t\text{-Na}_3\text{SbS}_4$. The resonance peaks attributed to the Sb–S vibrations of the isolated SbS_4 group are observed over the measured range. The peaks at $402 (\nu_a)$, $382 (\nu_a)$, and $359 (\nu_s) \text{ cm}^{-1}$ are assigned to the stretching vibration modes and those at $189 (\delta_E)$ and $155 (\delta_F) \text{ cm}^{-1}$ are assigned to the deformational vibration modes of Sb–S.^[31] Hence, the pure $t\text{-Na}_3\text{SbS}_4$ electrolyte is synthesized through liquid-phase reac-

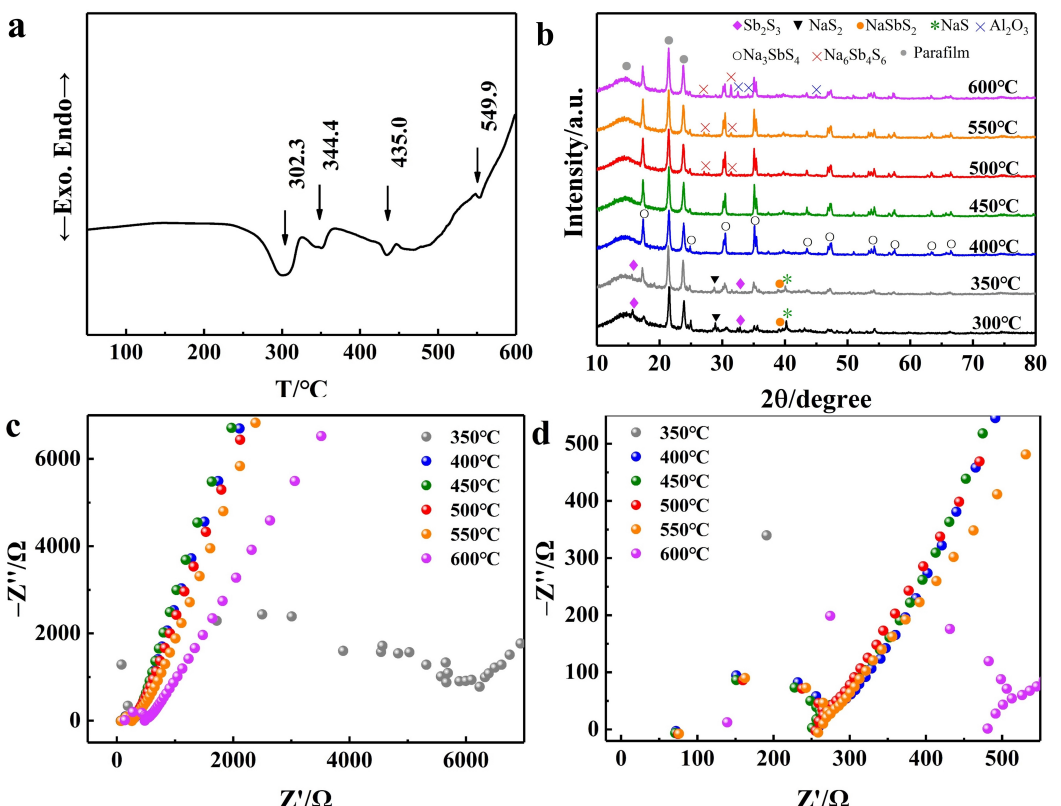


Figure 3. a) DSC curve of precursor, b) XRD patterns and c and d) Nyquist plots of precursors after heat-treated for different temperatures.

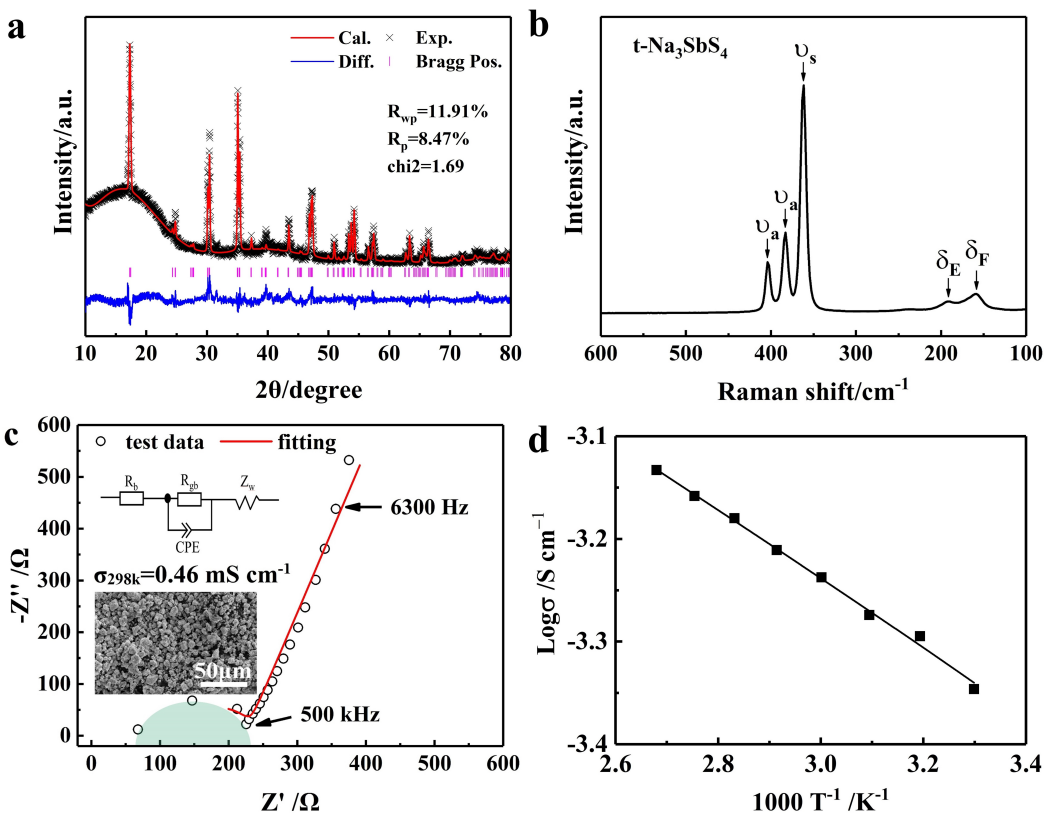


Figure 4. a) Rietveld refinement, b) Raman spectrum, c) Nyquist plots and a schematic diagram of the equivalent circuit employed in the simulation (the insert SEM image presents the morphology of $t\text{-Na}_3\text{SbS}_4$ with the even particle radius of $10\ \mu\text{m}$), d) Arrhenius plots of the $t\text{-Na}_3\text{SbS}_4$ solid electrolyte.

tion using ACN. The ionic conductive property of $t\text{-Na}_3\text{SbS}_4$ is measured using pellet sandwiched between two ion-blocking electrodes by electrochemical impedance spectroscopy (EIS) at 25°C . The Nyquist plots and the corresponding equivalent circuit are shown in Figure 4(c). The impedance spectra contain a semicircle in the high frequency attributed to the grain boundary resistance (R_{gb}) and a sloped line in the low frequency denoting Warburg resistance (Z_w), which is associated with capacitive behavior similar to the blocking electrodes. The intercept of the semicircle with the real axis at high frequency represents the bulk resistance (R_b). The total resistance (R_t) equals the sum of R_{gb} and R_b .^[8,40–42] The room ionic conductivity determined from the total resistance is $0.46\ \text{mS}\ \text{cm}^{-1}$,^[13] which is closed related to the small particle radius of $t\text{-Na}_3\text{SbS}_4$ (inset SEM image in Figure 4c). And the Arrhenius plots of the ionic conductivities for $t\text{-Na}_3\text{SbS}_4$ electrolyte versus temperatures are shown in Figure 4(d). The ionic conductivity obeys the Arrhenius law, and the activation energy is calculated to be $23.37\ \text{kJ}\ \text{mol}^{-1}$ based on Arrhenius plots using the conductivity values measured in the temperatures range from $30\text{--}100^\circ\text{C}$.

To further understand the effect of liquid-phase reaction time on precipitation, the precipitations at different reaction times are dried and heated treatment at 450°C , which are tested using Raman and XRD characterizations. The Raman spectra are shown in Figure 5(a). The bands attributed to SbS_4 group are observed over the four samples and the intensity

increases with a reaction time of liquid-phase reaction. Consistent with the XRD patterns in Figure 5(b), the characteristic peaks of $t\text{-Na}_3\text{SbS}_4$ gradually increase with the reaction time. Indicating that sodium polysulfide and Sb_2S_3 in the precipitation are all transformed into $t\text{-Na}_3\text{SbS}_4$. The resonance peaks for raw material Sb_2S_3 at 313 and $341\ \text{cm}^{-1}$ in Raman spectra (Figure 5a) are disappearing gradually with reaction time, showing that the contents of sulfur and sodium in the supernatant decreased with liquid-phase reaction time. Therefore, the content of unreacted Sb_2S_3 in the precipitate decreased after heat treatment. After 24 h of liquid-phase reaction, all components containing sodium, antimony and sulfur are in the precipitate, which converts to $t\text{-Na}_3\text{SbS}_4$ after heat treatment at 450°C . The electrochemical stability window of the $t\text{-Na}_3\text{SbS}_4$ electrolytes is evaluated with cyclic voltammetry (CV) measurement, as depicted in Figure 5(c). The scanning potentials are set from -1 to $5\ \text{V}$ vs. Na/Na^+ at a scan rate of $0.5\ \text{mV}\ \text{s}^{-1}$. Typical sodium deposition and dissolution peaks around $0\ \text{V}$ vs. Na/Na^+ are observed.^[43,44] An irreversible reaction at $0.5\ \text{V}$ is occurred in the first cycle and disappears in the following two cycles, which is beneficial for the formation of a stable $t\text{-Na}_3\text{SbS}_4/\text{Na}$ interface. In addition, no significant oxidation peak is detected from 1 to $5\ \text{V}$, indicating that $t\text{-Na}_3\text{SbS}_4$ exhibits a broad electrochemical stability window of $1\text{--}5\ \text{V}$. The cyclic stability of $t\text{-Na}_3\text{SbS}_4$ electrolytes against a metallic Na anode is evaluated using a $\text{Na}/t\text{-Na}_3\text{SbS}_4/\text{Na}$ symmetric cell at a constant current of $0.1\ \text{mA}\ \text{cm}^{-2}$. As

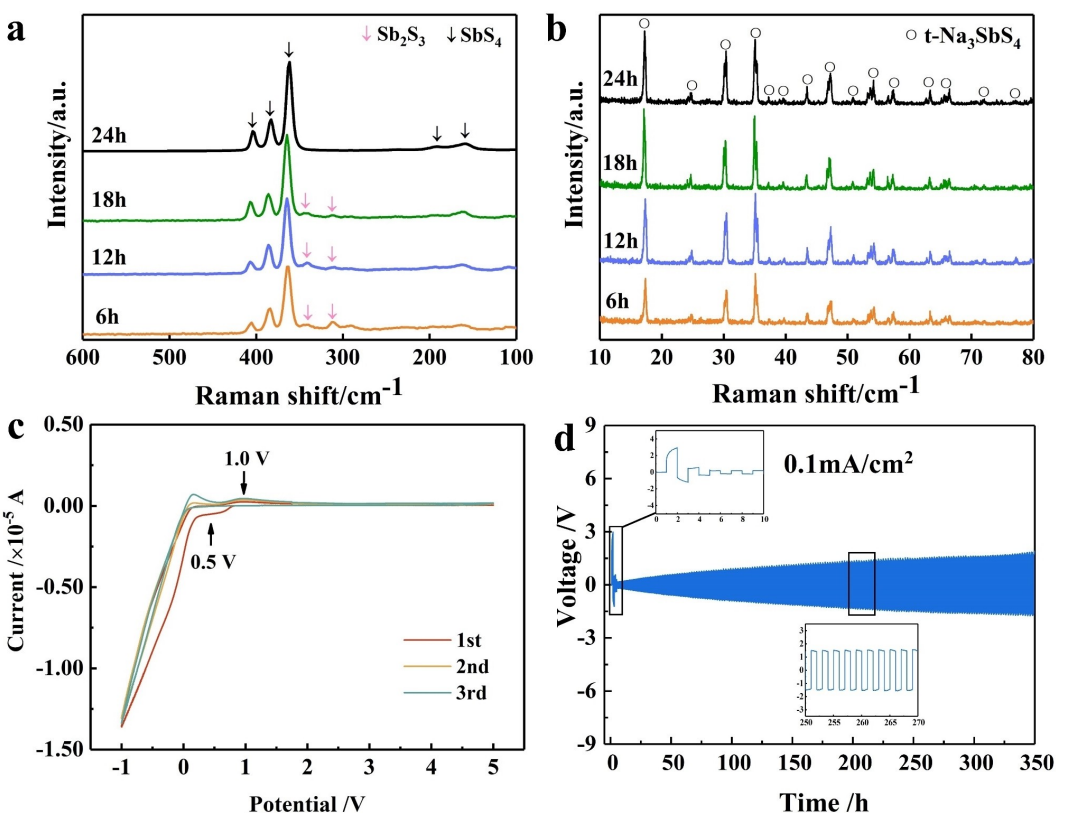


Figure 5. a) Raman spectra and b) XRD patterns of powder precipitates with different reaction times of 6, 12, 18 and 24 h after evaporation of ACN and heat treatment at 450 °C, c) Cyclability of t-Na₃SbS₄ in a symmetric Na/t-Na₃SbS₄/Na cell with a current density of 0.1 mA cm⁻² at room temperature, d) cyclic voltammogram curve of a Na/t-Na₃SbS₄/stainless steel cell between -1 and 5 V (vs. Na/Na⁺).

depicted in Figure 5(d), In the first cycle, high voltage spike corresponding to the irreversible reduction reaction in the first circle of CV is observed. Subsequently, the cell shows sluggish increase of polarization voltage and operates for over 300 h, displaying a satisfactory cycle performance toward Na metal.

Figure 6(a) shows the particle size distribution of t-Na₃SbS₄, and the inset is the SEM image. Regular shape and a relatively narrow distribution with an average particle size of 10.85 μm can be observed. The EDS spectrums in Figure 6(b) indicate that all of the component elements are homogeneously distributed throughout the electrolyte. Smaller particles and morphological homogeneity are closely associated with increasing ionic conductivity. The Sb-based sulfide electrolytes possess outstanding ambient environment stability and the generation of toxic H₂S gas is negligible. This stability closely follows the hard and soft acids and bases (HSAB) theory,^[34,31] the element antimony in the Sb-based sulfide electrolyte is a soft acid and reacts preferentially to the sulfur (soft base) rather than to the oxygen (hard base) in the air, thus H₂S is rarely produced. In contrast, most thiophosphate-themed conductors are unstable against oxygen because phosphorus is a hard acid that reacts preferentially with oxygen rather than sulfur, leading to the release of H₂S gas and a significant reduction in the ionic conductivity of the solid electrolytes. To clarify the air stability of the as-prepared t-Na₃SbS₄, the powder sample is exposed to ambient atmosphere for 48 h (humidity 8%). The XRD patterns

of the inert atmosphere-preserved t-Na₃SbS₄ and the air-exposed t-Na₃SbS₄ are shown in Figure 6(c). Actually, the sample absorbing moisture in highly humid environment will result in the formation of Na₃SbS₄·9H₂O.^[34] However, in this experiment, there are minor XRD peaks variation can be observed for the air-exposed t-Na₃SbS₄, which may be due to the small amount of water absorption. The change can be observed in Nyquist plots (Figure 6d), the ionic conductivity of air-exposed t-Na₃SbS₄ slightly drops to 0.027 mS cm⁻¹, consistent with the result of XRD. It is worth mentioning that by reheating the air-exposed sample at 200 °C for 2 h, the t-Na₃SbS₄ phase can be regained, which can be observed in XRD patterns and Nyquist plots (illustration of purple profiles). The same impedance values for the two samples suggest the air stability of as-prepared t-Na₃SbS₄. This fact further confirms that soft acids Sb can strongly bind with soft base S in t-Na₃SbS₄, therefore the chemical stability of t-Na₃SbS₄ in ambient environment is improved.

Fabricating thin solid electrolyte membranes have the foremost significance for practical all-solid-state sodium-ion batteries. Therefore, t-Na₃SbS₄ powder electrolytes and 5/2% polytetrafluoroethylene (PTFE) are calendared to prepare the membranes, respectively. The optical images of the prepared electrolyte membrane are shown in Figure 7(a and b). Promising maneuverability and good ductility can be observed since the composite electrolyte membrane can be folded without

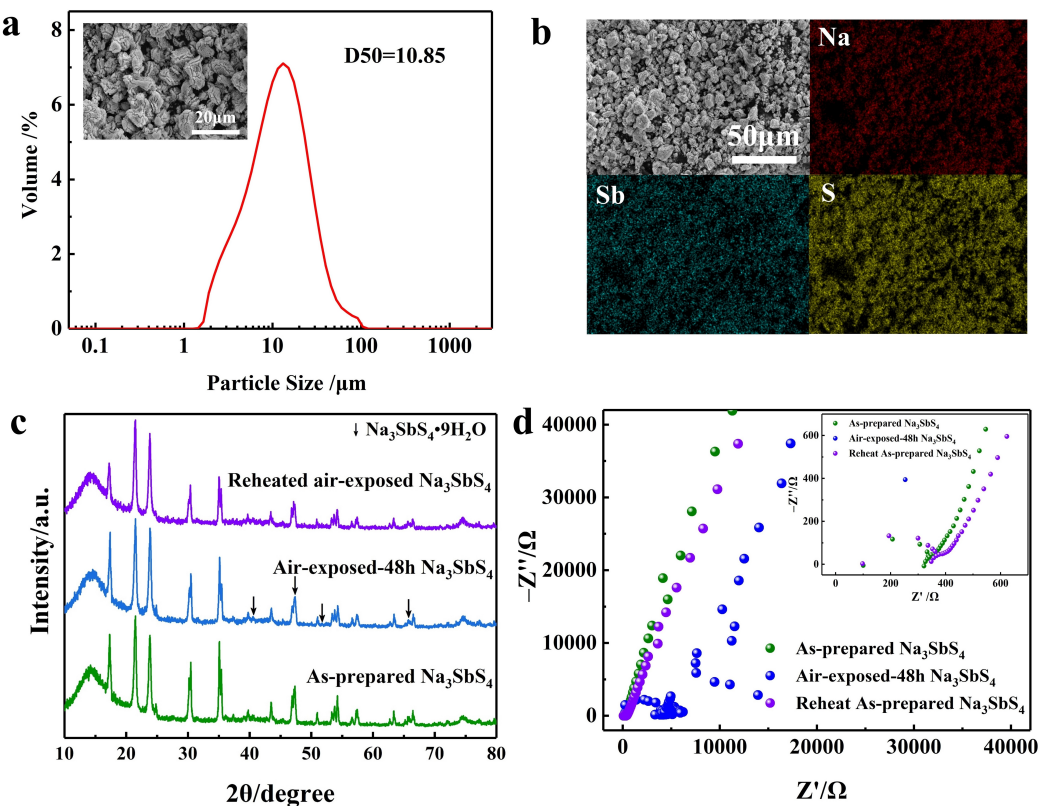


Figure 6. a) Particle size distribution curve of t-Na₃SbS₄ (the inset is the SEM image of t-Na₃SbS₄), b) EDS mappings of Na, Sb, and S elements for as-prepared t-Na₃SbS₄, c) XRD patterns, and d) Nyquist plots of as-prepared t-Na₃SbS₄, air-exposed-48 h t-Na₃SbS₄ (humidity 8%), and reheated air-exposed t-Na₃SbS₄ sample (200 °C for 2 h under vacuum).

breaking. The surface SEM image (Figure 7c) highlights the compactness in morphology. The EDS images (Figure 7d) show the uniform distributions of Na, Sb, S (t-Na₃SbS₄), and F (PTFE) filling the pore spaces between the particles of t-Na₃SbS₄ to provide good binding energy. The thickness of 170 ± 10 μm can be observed in the cross-sectional SEM image shown in Figure 7(e). The high magnification cross-sectional SEM (Figure 7f) indicates the PTFE and powder electrolyte are well mixed and PTFE acts as a good bonding agent. Although the additions of 2% and 5% PTFE binders to the electrolytes cause negligible changes in XRD patterns (Figure 7g), the decrease of ion conductivity with PTFE contents can be observed in Figure 7(h) and may be due to the weak ionic conductivity capability of the binder (the ion conductivities of solid electrolytes with 5% and 2% PTFE are 0.016 and 0.17 mS cm⁻¹, respectively). Although the ionic conductivity of t-Na₃SbS₄ and PTFE composite electrolyte membrane is slightly lower than t-Na₃SbS₄, which still fulfills the requirement of all-solid-state sodium batteries. The Arrhenius plots of conductivities of membrane versus temperatures are shown in Figure 7(i), and the calculated activation energy is 5.6 kJ mol⁻¹. The fibrous PTFE provides an effective bridge for the tight connection of the sulfide powder electrolytes and relieves the internal stress of the t-Na₃SbS₄ electrolyte, facilitating outstanding mechanical strength and transport properties for electrolytes.

Conclusion

In summary, t-Na₃SbS₄ solid electrolyte is successfully prepared by liquid-phase reaction using ACN and subsequently heat treatment in this work. More importantly, the influence of stirring time on the liquid-phase reaction process and the effect of post-temperature on the generation of t-Na₃SbS₄ are extensively investigated. The as-synthesized electrolyte presents a small particle size, uniform particle size distribution, and high ionic conductivity of 0.46 mS cm⁻¹ at room temperature. By exposing the t-Na₃SbS₄ electrolyte to a less-humid condition, no obvious crystal structure change and little ionic conductivity decrease can be observed after reheating at 200 °C, illustrating the superiority of the antimony-based electrolytes. Furthermore, this work demonstrates a solvent-free method for fabricating ultrathin solid electrolyte, which exhibits excellent mechanical bendability and ionic conductivity. We believe that this technology would be a feasible and cost-effective mean of transferring all-solid-state sodium-ion battery technology from the laboratory to the factory.

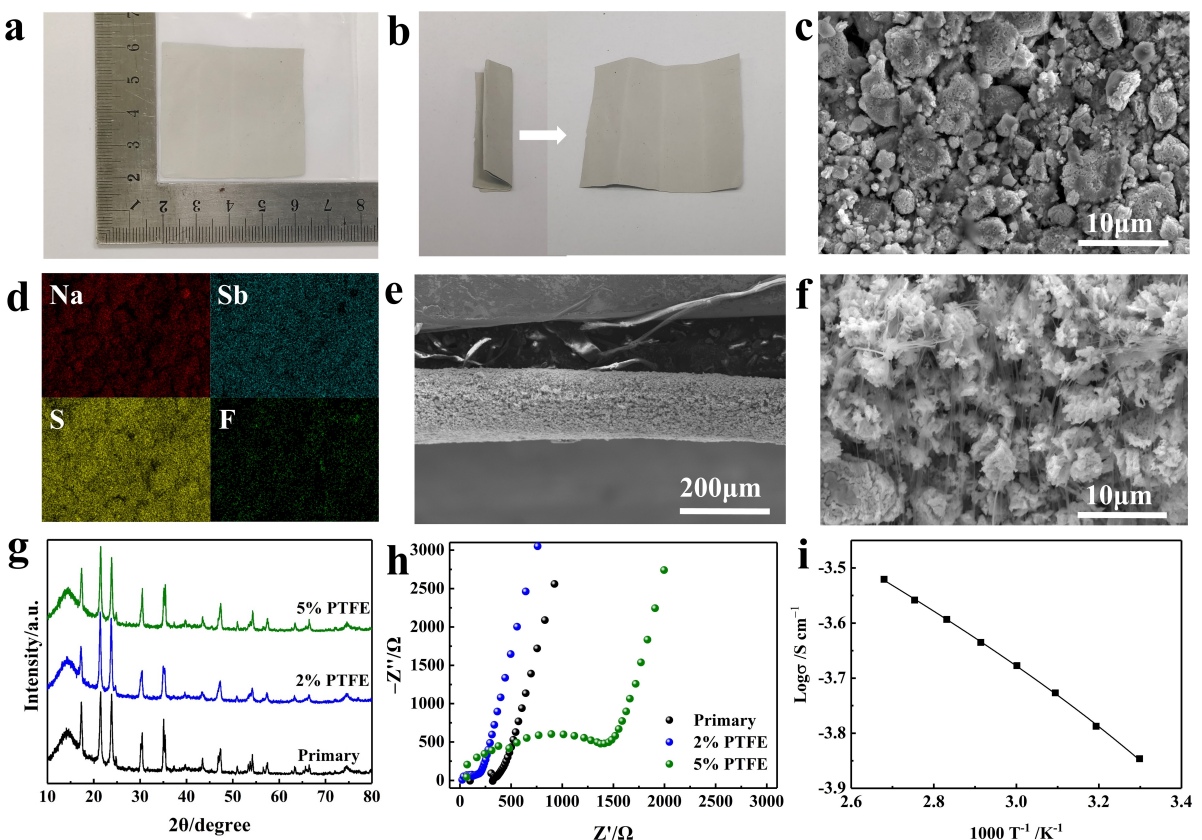


Figure 7. a, b) The optical photographs of PTFE and t-Na₃SbS₄ electrolyte composite membranes. c) Surface SEM image and d) EDS mappings of Na, Sb, S, and F elements for membrane. e) Lower-magnification and f) higher-magnification images of cross-sectional SEM. g) XRD patterns and h) Nyquist plots of the primary electrolyte powder and electrolyte membranes with different amounts of PTFE. i) Arrhenius plots of electrolyte membrane with 2% PTFE.

Experimental Section

Preparation of Na₃SbS₄ electrolyte by liquid-phase reaction using acetonitrile

Na₃SbS₄ sulfide solid electrolyte was synthesized using Na₂S (95%, Aladdin), Sb₂S₃ (99.99%, Aladdin), and sulfur (99.98%, Aldrich) powders. Polar aprotic solvent acetonitrile (ACN, 99.8%, anhydrous grade, Aladdin) was used as the solvent. All materials were not further purified. Firstly, A stoichiometric amount of Na₂S, Sb₂S₃, and S (3:1:2 in molar ratio) was ground in an agate mortar and then poured into ACN solvent. The mass-to-volume ratio of powder:solvent was 3:20 g mL⁻¹. The mixed solution was then heated and stirred at 50 °C for 24 h. After the reaction, the solution was centrifuged at 4000 rpm for 5 min to separate powder precipitate, which then was dried at 50 °C for 12 h to obtain the precursor of Na₃SbS₄. Subsequently, the powders were heated by a muffle furnace in the glove box at different temperatures for 3 h to obtain the pure Na₃SbS₄ electrolytes. All the above processes were carried out under Ar atmosphere because the sulfide electrolyte easily reacts with moisture in the air.

Preparation of Na₃SbS₄ electrolyte membrane

Na₃SbS₄ solid electrolyte and polytetrafluoroethylene (PTFE) were weighed into an agate mortar and thoroughly mixed until a dough was formed. Then the malleable dough was repeatedly folded and calendered with a roller to form a desirable thickness electrolyte.

Materials characterizations

The particle size distribution of t-Na₃SbS₄ electrolyte after heat treatment was measured with a particle size analyzer (Malvern Mastersizer 2000). Powder X-ray diffraction (XRD) measurement was performed using a Rigaku D/max-2500 equipped with Cu-K α radiation from 10° to 80°, during which the samples were sealed with Parafilm. The typical morphology and structure were observed by the field-emission scanning electron microscopy (SEM, MERLIN Compact, ZEISS, Germany) equipped with energy-dispersive X-ray spectroscopy (EDS). Raman scattering measurement (HORIBA EVOLUTION; HORIBA JOBIN YVON S.A.S.) was conducted using a Renishaw Invia system at an excitation of 532 nm. Differential Scanning Calorimetry (DSC) profile was detected by the Perkin-Elmer DSC8000 from room temperature to 600 °C with a scan rate of 10 °C min⁻¹.

Electrochemical measurements

Electrochemical impedance spectroscopy (EIS) spectra were recorded using an electrochemical workstation (IM6ex, Zahner) in the frequency range of 1–10⁶ Hz with an amplitude of 10 mV. The ionic conductivity of Na₃SbS₄ was calculated through the equation: $\sigma = d/AR$, where d is the pellet thickness, A is the pellet area, and R is the pellet resistance. The electrolyte pellets for the measurement were cold-pressed from as-synthesized powders at 360 MPa pressure in teflon tubes with an inner diameter of 10 mm. Two stainless-steel sheets were used as blocking electrodes. Temperature-dependent conductivities measurements were performed from room temperature to 100 °C. The cycle stability of the Na₃SbS₄

was studied with symmetric cells of the type Na/Na₃SbS₄/Na using a LAND CT-2001A instrument at a current density of 0.1 mA cm⁻². The electrochemical stability window of the Na₃SbS₄ solid electrolyte was evaluated by cyclic voltammetry (CV) measurement, and a Na/Na₃SbS₄/stainless steel cell was assembled and tested on an electrochemical workstation (PMC1000/ DC, Princeton) between -1 and 5 V at a scan rate of 0.5 mVs⁻¹.

Acknowledgements

This work was financially supported by the Science & Technology Development Fund of Tianjin Education Commission for Higher Education (2018KJ127).

Conflict of Interest

The authors declare that they have no known competing financial interests or personal relationships that could have appeared to influence the work reported in this paper.

Data Availability Statement

Research data are not shared.

Keywords: electrolyte membrane · liquid-phase reaction · N · bS₄ sulfide solid e · troylyte · reaction mechanisms · sodium

- [1] H. Cao, M. Yu, L. Zhang, Z. Zhang, X. Yan, P. Li, C. Yu, *J. Mater. Sci. Technol.* **2021**, *70*, 168–175.
- [2] W. Weng, G. Liu, Y. Li, L. Shen, X. Yao, *Appl. Mater. Today* **2022**, *27*, 101448.
- [3] R. Jalem, B. Gao, H. K. Tian, Y. Tateyama, *J. Mater. Chem. A* **2022**, *10*, 2235–2248.
- [4] Q. Zhang, Q. Zhou, Y. Lu, Y. Shao, Y. Qi, X. Qi, G. Zhong, Y. Yang, L. Chen, Y. S. Hu, *Engineering-Pr* **2022**, *8*, 170–180.
- [5] Y. Fujita, A. Nasu, A. Sakuda, M. Tatsumisago, A. Hayashi, *J. Power Sources* **2022**, *532*, 231313.
- [6] Q. Zhou, L. Wang, W. Li, S. Zeng, K. Zhao, Y. Yang, Q. Wu, M. Liu, Q. A. Huang, J. Zhang, X. Sun, *ACS Appl. Mater. Interfaces* **2021**, *13*, 25036–25043.
- [7] F. Sun, Y. Xiang, Q. Sun, G. Zhong, M. N. Banis, Y. Liu, R. Li, R. Fu, M. Zheng, T. Sham, Y. Yang, X. Sun, X. Sun, *Adv. Funct. Mater.* **2021**, *31*, 2102129.
- [8] G. Liu, X. Sun, X. Yu, W. Weng, J. Yang, D. Zhou, R. Xiao, L. Chen, X. Yao, *Chem. Eng. J.* **2021**, *420*, 127692.
- [9] F. Tsuji, A. Nasu, A. Sakuda, M. Tatsumisago, A. Hayashi, *J. Power Sources* **2021**, *506*, 230100.
- [10] Y. Shao, G. Zhong, Y. Lu, L. Liu, C. Zhao, Q. Zhang, Y. S. Hu, Y. Yang, L. Chen, *Energy Storage Mater.* **2019**, *23*, 514–521.
- [11] S. Teragawa, K. Aso, K. Tadanaga, A. Hayashi, M. Tatsumisago, *J. Mater. Chem. A* **2014**, *2*, 5095–5099.
- [12] Z. Wang, L. Zhang, X. Shang, W. Wang, X. Yan, C. Yu, L. Wang, *Chem. Eng. J.* **2022**, *428*, 132094.
- [13] L. Shen, S. Deng, R. Jiang, G. Liu, J. Yang, X. Yao, *Energy Storage Mater.* **2022**, *46*, 175–181.
- [14] W. Weng, H. Wan, G. Liu, L. Wu, J. Wu, X. Yao, *ACS Appl. Energ. Mater.* **2021**, *4*, 1467–1473.
- [15] Y. Wang, D. Lu, M. Bowden, P. Z. El Khoury, K. S. Han, Z. D. Deng, J. Xiao, J. G. Zhang, J. Liu, *Chem. Mater.* **2018**, *30*, 990–997.
- [16] K. Noi, K. Suzuki, N. Tanibata, A. Hayashi, M. Tatsumisago, *J. Am. Ceram. Soc.* **2018**, *101*, 1255–1265.
- [17] H. Wan, L. Cai, W. Weng, J. P. Mwizerwa, J. Yang, X. Yao, *J. Power Sources* **2020**, *449*, 227515.
- [18] F. Tsuji, S. Yubuchi, A. Sakuda, M. Tatsumisago, A. Hayashi, *J. Ceram. Soc. Jpn.* **2020**, *128*, 641–647.
- [19] W. Weng, G. Liu, L. Shen, X. Yao, *J. Power Sources* **2021**, *512*, 230485.
- [20] S. Xiong, Z. Liu, H. Rong, H. Wang, M. McDaniel, H. Chen, *Sci. Rep.* **2018**, *8*, 9146.
- [21] H. Wan, J. P. Mwizerwa, F. Han, W. Weng, J. Yang, C. Wang, X. Yao, *Nano Energy* **2019**, *66*, 104109.
- [22] N. H. H. Phuc, K. Morikawa, T. Mitsuhiro, H. Muto, A. Matsuda, *Ionics* **2017**, *23*, 2061–2067.
- [23] R. C. Xu, X. H. Xia, Z. J. Yao, X. L. Wang, C. D. Gu, J. P. Tu, *Electrochim. Acta* **2016**, *219*, 235–240.
- [24] Z. Liu, W. Fu, E. A. Payzant, X. Yu, Z. Wu, N. J. Dudney, J. Kiggans, K. Hong, A. J. Rondinone, C. Liang, *J. Am. Chem. Soc.* **2013**, *135*, 975–978.
- [25] X. Yao, D. Liu, C. Wang, P. Long, G. Peng, Y. S. Hu, H. Li, L. Chen, X. Xu, *Nano Lett.* **2016**, *16*, 7148–7154.
- [26] Z. Zhang, H. Cao, L. Zhang, *J. Mater. Sci.* **2021**, *56*, 10565–19574.
- [27] T. Ando, A. Sakuda, M. Tatsumisago, A. Hayashi, *Electrochim. Commun.* **2020**, *116*, 106741.
- [28] H. Gamo, N. H. H. Phuc, H. Muto, A. Matsuda, *ACS Appl. Energ. Mater.* **2021**, *4*, 6125–6134.
- [29] H. Gamo, H. H. P. Nguyen, R. Matsuda, H. Muto, A. Matsuda, *Solid State Ionics* **2020**, *344*, 115133.
- [30] S. Yubuchi, A. Ito, N. Masuzawa, A. Sakuda, A. Hayashi, M. Tatsumisago, *J. Mater. Chem. A* **2020**, *8*, 1947–1954.
- [31] L. Zhang, D. Zhang, K. Yang, X. Yan, L. Wang, J. Mi, B. Xu, Y. Li, *Adv. Sci.* **2016**, *3*, 1600089.
- [32] Q. Zhang, C. Zhang, Z. D. Hood, M. Chi, C. Liang, N. H. Jalarvo, M. Yu, H. Wang, *Chem. Mater.* **2020**, *32*, 2264–2271.
- [33] A. Banerjee, K. H. Park, J. W. Heo, Y. J. Nam, C. K. Moon, S. M. Oh, S. T. Hong, Y. S. Jung, *Angew. Chem. Int. Ed.* **2016**, *128*, 9786–9790.
- [34] H. Wang, Y. Chen, Z. D. Hood, G. Sahu, A. S. Pandian, J. K. Keum, K. An, C. Liang, *Angew. Chem. Int. Ed.* **2016**, *128*, 8693–8697.
- [35] D. Zhang, X. Cao, D. Xu, N. Wang, C. Yu, W. Hu, X. Yan, J. Mi, B. Wen, L. Wang, L. Zhang, *Electrochim. Acta* **2018**, *259*, 100–109.
- [36] K. H. Park, D. H. Kim, H. Kwak, S. H. Jung, H. J. Lee, A. Banerjee, J. H. Lee, Y. S. Jung, *J. Mater. Chem. A* **2018**, *6*, 17192–17200.
- [37] H. Gamo, N. H. H. Phuc, R. Matsuda, H. Muto, A. Matsuda, *Mater. Today Energy* **2019**, *13*, 45–49.
- [38] M. Uematsu, S. Yubuchi, K. Noi, A. Sakuda, A. Hayashi, M. Tatsumisago, *Solid State Ionics* **2018**, *320*, 33–37.
- [39] Z. Wang, Y. Jiang, J. Wu, Y. Jiang, S. Huang, B. Zhao, Z. Chen, J. Zhang, *Chem. Eng. J.* **2020**, *393*, 124706.
- [40] S. Takeuchi, K. Suzuki, M. Hirayama, R. Kanno, *J. Solid State Chem.* **2018**, *265*, 353–358.
- [41] J. Yang, H. L. Wan, Z. H. Zhang, G. Z. Liu, X. X. Xu, Y. S. Hu, X. Y. Yao, *Rare Met.* **2018**, *37*, 480–487.
- [42] L. Zhang, K. Yang, J. Mi, L. Lu, L. Zhao, L. Wang, Y. Li, H. Zeng, *Adv. Energy Mater.* **2015**, *5*, 1501294.
- [43] H. Wang, Y. Chen, Z. D. Hood, G. Sahu, A. S. Pandian, J. K. Keum, K. An, C. Liang, *Angew. Chem. Int. Ed.* **2016**, *55*, 8551–8555; *Angew. Chem.* **2016**, *128*, 8693–8697.
- [44] W. Weng, H. Wan, G. Liu, L. Wu, J. Wu, X. Yao, *ACS Appl. Energ. Mater.* **2021**, *4*, 1467–1473.

Manuscript received: August 26, 2022

Revised manuscript received: October 30, 2022

Version of record online: November 18, 2022